Elastic localisation with particular reference to tape-springs

J A Clarkson & K A Seffen

jac287@cam.ac.uk, kas14@cam.ac.uk

Advanced Structures Group, Civil Engineering Building, Department of Engineering, University of Cambridge, CB3 0FA

Abstract

Many elastic systems localise under applied displacement, precipitating into regions of lower and higher strain; further displacement is accommodated by growth of the high strain region at a constant load. Such systems can be studied as propagating instabilities, focusing on the work required to propagate the high strain region, or as two-phase energy minimisation problems. It is shown that the Maxwell "Equal-Areas" Construction, and the related Common Tangent Construction, provide the solution to either approach. A new, graphical, proof of the Maxwell Equal-Areas Construction using total strain energy diagrams is presented. Tape-springs are investigated as a case study, with localisation presenting as the formation of elastic folds—developable regions with high curvature. One notable property of tape-spring folds is that the fold radius is approximately equal to the initial transverse radius. This result was first proven by Rimrott, and later improved by Calladine & Seffen. A further improvement is obtained here by application of the Common Tangent Construction, and all solutions are shown to be approximations to the Maxwell Equal-Areas Construction in the limit of zero thickness.

Keywords: tape-spring, deployable structures, shell, localisation, folded hinge, Maxwell construction

Nomenclature

$\sigma =$ generalised stress
$\epsilon =$ generalised strain
$u =$ strain energy per unit length
$U =$ total strain energy
$r =$ transverse radius of relaxed tape
$\alpha =$ angle subtended by tape cross-section
$b =$ transverse width of tape, equal to $r\alpha$
$h =$ thickness of tape
$E =$ Young's modulus
$\nu =$ Poisson's ratio
$D =$ plate flexural stiffness, $Eh^3/12(1-\nu^2)$
$\kappa_x =$ longitudinal curvature
$\kappa_y =$ transverse curvature
$M =$ section bending moment, parallel to y axis
$\Theta =$ total angle subtended in bending
$\beta =$ non dimensional parameter comparing plate like versus beam like bending, rh/b^2
$T =$ equivalent non dimensional parameter, equal to $1/\sqrt{\beta}$

1 Introduction

Many elastic systems display localisation, where uniform deformation gives way to deformation in two distinct regions of differing strain. Examples include the inflation of long balloons, the buckling of beams on elastic foundations, and the folding of tape-springs, to which particular reference will be made in this paper. Common to these systems is a characteristic "up-down-up" generalised load-displacement relationship between the problem-specific work-conjugate variables, e.g. stress-strain or moment-curvature.

There are clear parallels with thermodynamic phase transitions, in which a second phase precipitates within the first as a result of a change in state; for example, the condensation of liquid droplets in a gas cooled to boiling point, where the new phase initially forms at a low volume fraction, which gradually increases to unity as the phase transition occurs.

Whilst thermodynamic phase transition problems deal with pressure and volume (or temperature), and elastic localisation deals with stress and strain, the underlying energetic principles are the same. In both cases, the two phase solution can be predicted using the Maxwell Equal-Areas Construction, first formulated by J C Maxwell in an 1875 lecture to the Chemical Society [1] on the liquid-to-gas phase transition predicted by the Van der Waals equation [2]. Figure 1 plots the Van der Waals equation for water at $T = 560\,\mathrm{K}$; Maxwell's Construction is shown through work arguments to be the horizontal line which satisfies $A_1 = A_2$, where A_1 and A_2 are the areas below and above this line, enclosed by the curve.

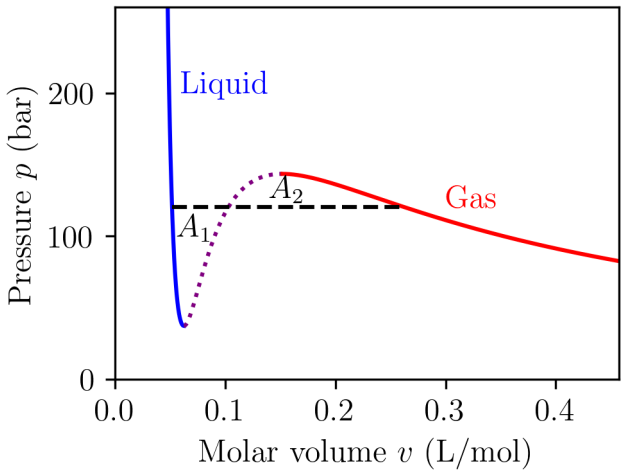

Figure 1: Van der Waals equation for water (dotted line indicating unstable region) with Maxwell Equal-Areas Construction applied.

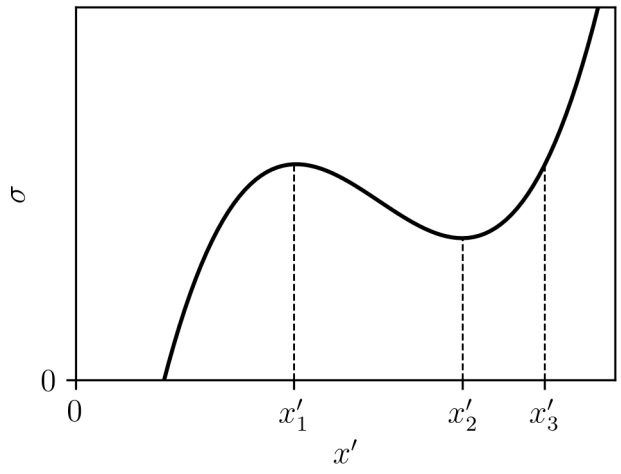

Figure 2: Ericksen bar stress strain curve [3]

Ericksen [3] was the first to consider localisation in the context of elastic systems, postulating a 1D "Ericksen bar" model obeying a non-monotonic stress-strain relationship (Fig. 2). Clearly the intermediate decreasing region ($x'_1 < x' < x'_2$) is unstable; under load control, there is a jump in strain from x'_1 to x'_3 as the load increases. By contrast, under *displacement* control, a two phase solution analogous to a Van der Waals fluid will occur if the mean strain lies within the unstable region, with phases predicted by the Maxwell Equal-Areas Construction.

That localisation occurs under displacement control and not load control is a key point; it should be noted that this analysis makes no predictions about where the phases will precipitate, only the

proportion of the elastic domain (in Ericksen's analysis, the overall lengths of the rod) in each phase. Later work [4] refined the model into a "regularised" Ericksen bar by incorporating penalty terms in the strain energy proportional to strain derivatives. These act as an interface energy, penalising transitions between phases thus encouraging the phases to coalesce; if the coefficients of the strain derivatives are given physically appropriate values then accurate predictions about precipitation locations can be made.

A long-standing problem in elastic localisation lies within the unique behaviour of open, transversely curved strips known as "tape-springs" [7]. They can be "folded" under moments applied to their ends, which localises into a fold region of high curvature, adjoined by regions low curvature, between which exists a "ploy" transition region. This problem has significant practical relevance due to the widespread use of tape-springs as deployable structures in aerospace applications [7] [20] [21] [22], where they are stored in a folded or coiled configuration: thus, we seek improved predictions of the fold curvature. We also aim to emphasise and clarify the relevance of the Maxwell construction to tape-spring folding; previous work [7] has utilised a "unit length" in their Maxwell construction analysis, we show this is not needed. In fact, the Maxwell construction is satisfied specifically on the boundary between the two phases—this has consequences for systems with spatially varying load displacement relationships, which we investigate with reference to varying cross-section tape-springs in a second paper.

By treating a tape-spring as an unregularised Ericksen bar, we assume, in effect, that the ploy transition region does not exist. While this is clearly false, we note, in line with previous work [5][6], that the ploy region is invariant under fold propagation, hence the associated strain energy can be neglected from any minimisation; for a full treatment of the ploy region, as part of a regularised Ericksen bar analogy, we refer the reader to Martin et.al [12].

The first section of this paper begins by summarising proofs for the Maxwell Equal-Areas Construction and the related Common Tangent Construction. A new proof showing how the Maxwell Equal-Areas Construction minimises the strain energy via graphical "strain energy diagrams" is also presented.

The second section considers the specific elastic localisation problem of a folding tape-spring. Existing analytical predictions of tape-spring fold radius by Rimrott [5], and Calladine & Seffen [6] are discussed and their relation to the Maxwell Equal-Areas Construction shown. An improved prediction is made by direct application of the Common Tangent Construction, and the analytical predictions are compared to more accurate, numerically solved finite element analyses.

2 Localisation

2.1 Propagating instability

Elastic localisation problems are also often termed "propagating instabilities", in reference to both the buckling of the system into the two phases, and to the accommodation of further displacement via the growth of the high strain phase. A familiar example is the inflation of a long rubber balloon by the progression of a bulge along the length. As anyone who attempts to blow up such a balloon knows, considerable effort is required to form the bulge in the first place, but once formed the rest of the balloon can be inflated with relative ease as the bulge progresses towards the other end. More precisely, a high pressure is required to form the bulge, which can then propagate at a lower, constant, pressure, as illustrated in Fig. 3.

By consideration of the balance of work internally and externally as the bulge propagates

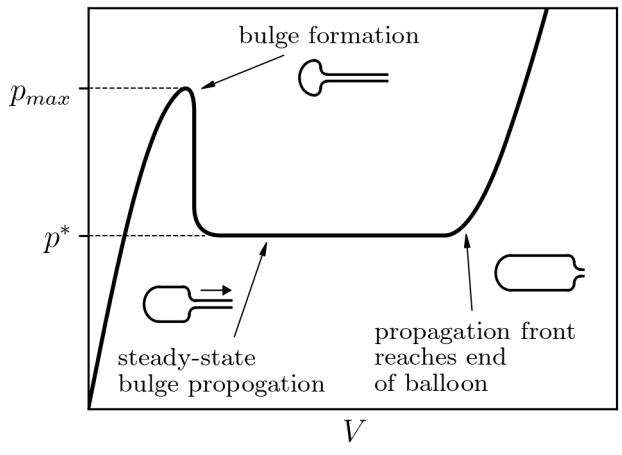

Figure 3: Balloon inflation pressure-volume relationship

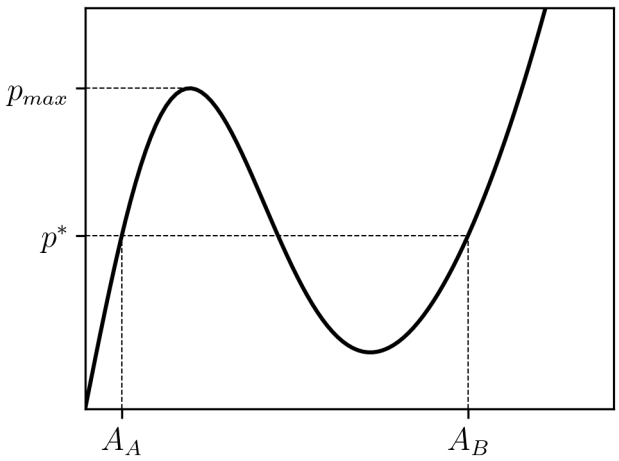

Figure 4: Balloon pressure-cross-sectional area relationship

through a small length δL along the balloon section, the propagation pressure can be obtained [8]. For example, a typical internal pressure-cross-sectional area relationship, denoted as $p(A)$, is shown in Fig. 4. The internal work as the length δL is stretched from area A_A to A_B is

$$\delta U_{\text{int}} = \delta L \int_{A_A}^{A_B} p \, \mathrm{d}A \tag{1}$$

This change in area produces an increase of volume $\delta V = (A_B - A_A)\delta L$: the external work done is therefore

$$\delta W_{\text{ext}} = p^*(A_B - A_A)\delta L \tag{2}$$

Equating internal and external work done leads to

$$\int_{A_A}^{A_B} p \, \mathrm{d}A = p^*(A_B - A_A) \tag{3}$$

where p^* is the bulge propagation pressure. Note that the analysis assumes that the transition region between the large and small diameter regions is a constant feature of the problem and does not affect the work balance: recent work by Lestringant & Audoly has accounted for this region in order to obtain a regularised balloon bulge propagation model (in the manner of a regularised Ericksen bar model) [9].

More broadly, for generalised stress and strain, we have

$$\int_{\epsilon_A}^{\epsilon_B} \sigma \, \mathrm{d}\epsilon = \sigma(\epsilon_B - \epsilon_A) \tag{4}$$

Note that this can only be satisfied for $\epsilon_A \neq \epsilon_B$ if the stress-strain relationship is non-linear and non-monotonic, which is a key requirement for all localisation problems, such as the $p - A$ curve in Fig. 4.

Equation 4 is simply the Maxwell Construction, which is also known as the Equal Areas Rule, as illustrated in Fig. 5: the propagation stress σ can be found by drawing a line such that the two areas above and below the line between the line and the stress-strain curve are equal: $A_1 = A_2$.

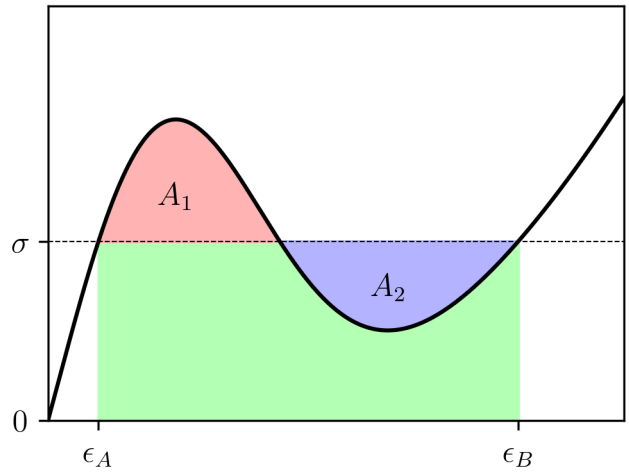

Figure 5: Maxwell Equal-Areas Construction for some general non-monotonic stress-strain relationship.

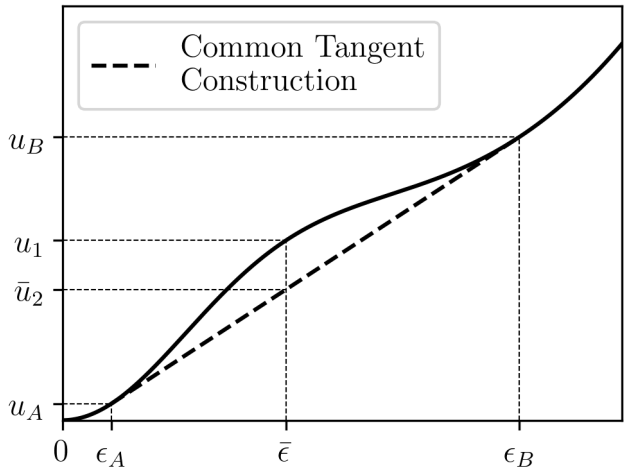

Figure 6: Strain energy per unit length, with the Common Tangent Construction applied

2.2 Common Tangent Construction

Alternatively, instead of considering the work required for propagation, the problem can be thought of as one of energy minimisation. Figure 6 is a representative plot of the strain energy per unit length, as a function of strain, obtained from integrating the stress-strain curve in Fig. 5. Let us examine the case of a rod loaded axially under displacement control.

Consider, first, a uniform strain $\bar{\epsilon}$ in the "bump" region between ϵ_A and ϵ_B in Fig. 6, resulting in a strain energy per unit length u_1, and total strain energy $U_1 = Lu_1$. If, instead, the strain splits into two phases, ϵ_A and ϵ_B, the total extension must remain unchanged, hence the lengths L_A and L_B of these regions must satisfy

$$\begin{aligned} e = L\bar{\epsilon} =& L_A\epsilon_A + L_B\epsilon_B \\ \bar{\epsilon} =& \gamma\epsilon_A + (1-\gamma)\epsilon_B \end{aligned} \tag{5}$$

where $\gamma = L_A/L$. Note that the uniform strain $\bar{\epsilon}$ can be thought of as the "mean strain" of the two phase solution. Similarly, the total two-phase strain energy U_2 can be written as a mean strain energy per unit length $\bar{u_2} = U_2/L$:

$$\begin{aligned} U_2 =& L_A u_A + L_B u_B \\ \bar{u_2} =& \gamma u_A + (1-\gamma) u_B \end{aligned} \tag{6}$$

Noting the identical forms between Eqns 5 & 6, a "lever rule" provides a graphical method to calculate $\bar{u_2}$: a straight line drawn between (ϵ_A, u_A) and (ϵ_B, u_B) on which lies the point $(\bar{\epsilon}, \bar{u_2})$, as illustrated in Fig. 6.

To compare the total strain energy of the single and two phase solutions one can instead compare the mean strain energies—clearly in Fig. 6, $\bar{u}_2 < u_1$, and is energetically preferred. The minimising energy is found by maximising the difference between u_1 and $\bar{u}_2$, which is obtained graphically by finding the tangent that touches the strain energy curve at two locations, thus providing the two phase strains and propagation stress σ (the gradient of the tangent).

This minimising condition is known as the "Common Tangent Construction", and is commonly encountered in Thermodynamics, for example, in determining the proportion of solid and liquid phases of a material via plots of Gibbs Free Energy. An algebraic statement of the graphical construction is

$$u_B - u_A = \left(\frac{\mathrm{d}u}{\mathrm{d}\epsilon}\right)_{\epsilon_A} (\epsilon_B - \epsilon_A) \tag{7}$$

Since $(\mathrm{d}u/\mathrm{d}\epsilon)_{\epsilon_A} = \sigma(\epsilon_A)$, this is clearly identical to the Maxwell Equal-Areas Construction given in Eqn 4.

2.3 Total strain energy diagrams

The following proof shows that the Maxwell Equal-Areas Construction automatically minimises the strain energy of two phases without recourse to the Common Tangent Construction. Consider the example stress-strain relationship from Fig. 5, with the strain energy per unit length given by the area under the curve. Now extend the curve sideways along a third "length" dimension to generate a stress-strain-length landscape, henceforth referred to as a "total strain energy" diagram.

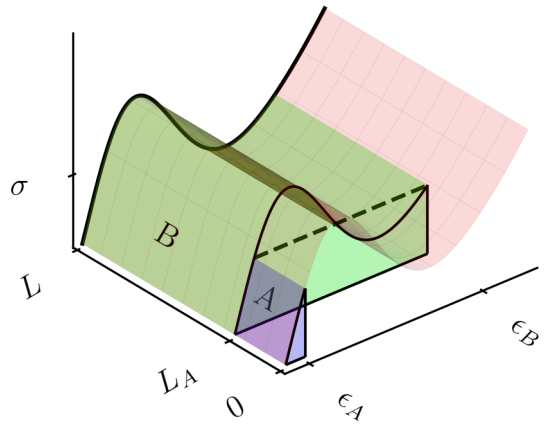

Figure 7: Total strain energy diagram

Figure 7 shows one such diagram. Let the length domain be divided into two phases; first phase A, of near zero strain representing a deformed but not-localised region, and second, B, of considerable strain which deforms as a localised region. The volumes underneath the surface in regions A and B gives the total strain energy in the system.

$$U = \int_0^{\epsilon_A} \sigma \,\mathrm{d}\epsilon L_A + \int_0^{\epsilon_B} \sigma \,\mathrm{d}\epsilon L_B \tag{8}$$

Additionally, the projection of these regions onto the horizontal plane gives the total displacement e of the system

$$e = L_A\epsilon_A + L_B\epsilon_B \tag{9}$$

Recalling that localisation occurs under displacement control, we seek to find the strains ϵ_A and ϵ_B which minimise the total strain energy for a given displacement e; in graphical terms, how

can the projected area be distributed between A and B, in order to minimise the volume, thus providing the equilibrium configuration?

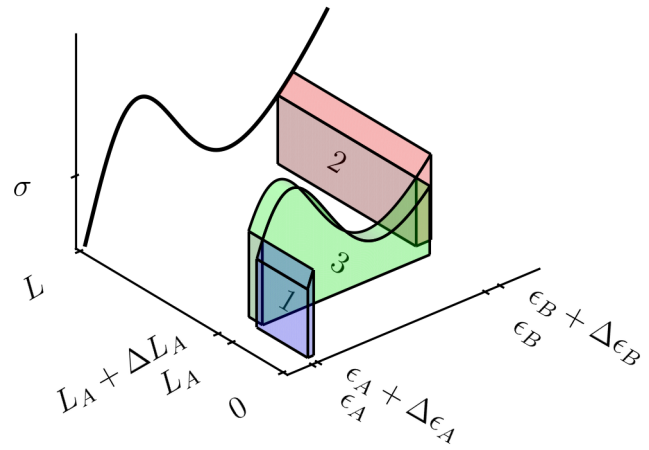

Figure 8: Change in volume for a small change in fold curvature

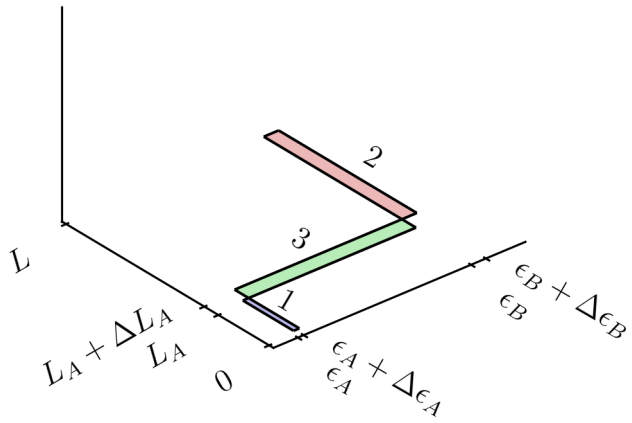

Figure 9: Change in areas

Consider $\Delta\epsilon_A$, as illustrated in Fig. 8; equilibrium dictates that the stress must be constant throughout the domain, necessitating a similar increase in ϵ_B. Under displacement control, the displacement e must remain constant, hence the length of the low strain region L_A must increase to ensure no change in projected areas. There are therefore three regions of change, numbered 1, 2 and 3: regions 1 and 2 are gained, and region 3 is lost. The constant displacement requirement means there is no change in vertically projected area, thus

$$A_1 + A_2 = A_3 \tag{10}$$

At the minimum strain energy, there should be no change in strain energy with an incremental change in ϵ_A. Therefore the total volume under the graph should be conserved, leading to

$$V_1 + V_2 = V_3 \tag{11}$$

Finally, noting in the limit as $\Delta\epsilon_A$ tends to zero

$$V_1 + V_2 = \sigma(A_1 + A_2) = \sigma A_3 \tag{12}$$

we arrive at

$$\sigma A_3 = V_3 \tag{13}$$

This can be written as

$$\sigma(\epsilon_B - \epsilon_A) = \int_{\epsilon_A}^{\epsilon_B} \sigma \, \mathrm{d}\epsilon \tag{14}$$

which is simply the Maxwell Equal-Areas Construction described previously.

2.4 Equivalence of two approaches

The propagating instability analysis and total strain energy minimisation analysis are two alternative ways to solve the same fundamental equation. Consider the total potential energy of the system Π defined

$$\Pi = U - W \tag{15}$$

where U is the internal strain energy and W the external work done. A small change in the total potential energy is given by

$$\mathrm{d}\Pi = \mathrm{d}U - \mathrm{d}W \tag{16}$$

Equilibrium of the system is satisfied when $\mathrm{d}\Pi = 0$. In the propagation analysis, external work is equated to internal work, thus $\mathrm{d}U = \mathrm{d}W$, hence satisfying $\mathrm{d}\Pi = 0$. The energy minimisation analysis occurs at a fixed extension, setting $\mathrm{d}W = 0$, and minimises the internal strain energy by setting $\mathrm{d}U = 0$, again satisfying $\mathrm{d}\Pi = 0$.

2.5 Phase separation

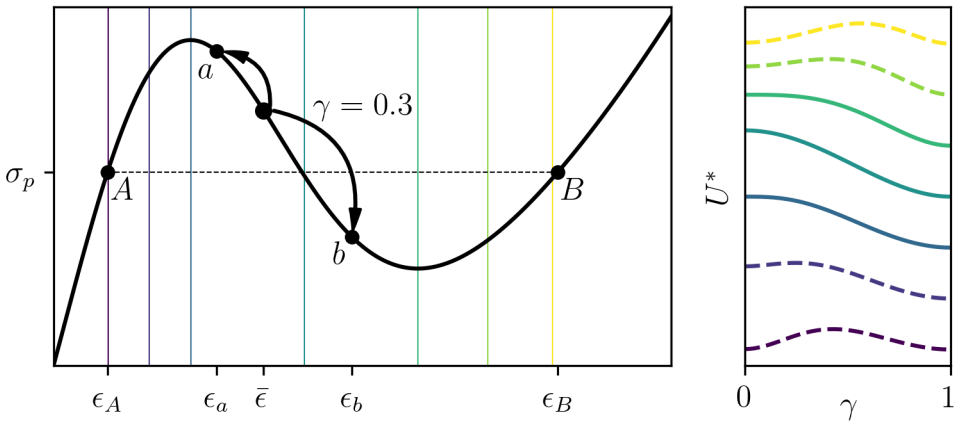

Figure 10: Phase separation process, and normalised strain energy for a range of mean strains. Dashed lines indicate bistable strain energy, solid lines monostable.

In order to localise and to achieve a lower strain energy, the single uniform phase must separate into two distinct phases. Consider the elastic domain at uniform strain $\bar{\epsilon}$, and let there be a small perturbation at some position along the domain, such that that point moves by Δx. This perturbation has split the domain into two phases, one, of length L_a and strain $\epsilon_a = \bar{\epsilon} - \Delta x/L_a$, and the other of length L_b a strain $\epsilon_b = \bar{\epsilon} + \Delta x/L_b$.

We know from the Common Tangent Construction that if $\epsilon_A < \bar{\epsilon} < \epsilon_B$, then a two phase solution with strains ϵ_A and ϵ_B gives the lowest possible strain energy. By varying Δx, it is possible to describe the process by which $\epsilon_a \to \epsilon_A$ and $\epsilon_b \to \epsilon_B$. This requires that $L_a = L_A$ and $L_b = L_B$. The ultimate value of Δx is given by

$$\begin{aligned} \Delta x_u =& L_A\bar{\epsilon} - L_A\epsilon_A \\ =& L_B\epsilon_B - L_B\bar{\epsilon} \end{aligned} \tag{17}$$

i.e. the difference between the single-phase and two-phase extension in regions A and B. Let $\gamma = \Delta x/\Delta x_u$ be a measure of the transition process, where substituting into the expressions for ϵ_a and ϵ_b leads straightforwardly to

$$\begin{aligned} \epsilon_a &= (1-\gamma)\bar{\epsilon} + \gamma\epsilon_A \\ \epsilon_b &= (1-\gamma)\bar{\epsilon} + \gamma\epsilon_B \end{aligned} \tag{18}$$

This process is inherently dynamic, as equilibrium is only guaranteed to be satisfied at $\gamma = 0$ and $\gamma = 1$. By calculating the strain energy as a function of γ, stability can be inferred. Fig. 10 shows an example of the separation process at $\gamma = 0.3$, and the strain energy U^* as a function of γ for the range of $\bar{\epsilon}$ given by the coloured vertical lines in the stress-strain plot. Note that the strain energy U^* has been normalised and scaled in order to best visualise the peaks and troughs. For $\bar{\epsilon}$ in the increasing σ region, the strain energy is bistable, with an energy barrier to overcome in order to transition to the two phase equilibrium. Thus phase separation will not spontaneously occur unless a large enough perturbation is provided—the single phase solution is *metastable*. Once $\bar{\epsilon}$ is in the decreasing σ region, the single phase solution is unstable and phase separation will spontaneously occur with the smallest perturbation.

This simple analysis neglects the strain energy associated with the boundary between the phases. Consideration of this interface energy will result in a slightly higher two phase strain energy, increasing the barrier to localisation while metastable, and rendering the two phase solution higher energy than the single-phase solution for a small range of $\bar{\epsilon} > \epsilon_A$.

3 Application to tape-springs

Tape-springs are long straight strips with transverse curvature, of which the carpenter's measuring tape is a familiar everyday example. Their cross-section is characterised by transverse radius r, subtended angle α, arc-width $b = \alpha r$, and shell thickness h, as illustrated in Fig. 11. A tape-spring can be bent along its length by applying equal and opposite rotations at either end. Equal-sense bending takes place when the induced curvature along the tape-spring is in the same direction as the initial transverse curvature; opposite-sense bending occurs otherwise. Under opposite-sense bending, a tape-spring will deform stiffly with uniform curvature up to a peak load, before buckling such that the curvature localises in a fold region characterised by high curvature and a flattened cross-section, and adjoined by relatively undeformed regions of low curvature. Between the folded and unfolded regions there exists a "ploy" region, where the cross-section gradually transitions from flattened to nearly undeformed. Further applied rotation is accommodated by growth of the fold region, which occurs at a constant moment.

Interestingly, the fold curvature is approximately equal to the initial transverse curvature, a feature first remarked upon by G T Bennett [11], and later proven by Rimrott [5], who noted that the cross-section in a fold is almost completely flat, enabling the simplifying assumption that $\kappa_y = 0$ (hence $\chi_y = 1/r$) across the width. A simple expression for the total strain energy store within the fold is then obtained and readily minimised.

Seffen & Pellegrino were the first to note that tape-spring folds can be classed as a propagating instability. Drawing a comparison with the balloon inflation problem, they suggested the fold curvature is governed by the same Maxwell Equal-Areas Construction, with $M(\kappa)$ in lieu of $p(A)$. More recently, Martin et.al [12] pointed out how the propagating instability model, as per Ericksen's original bar model, does not predict the location of folds or the behaviour of the ploy transition region between folded and unfolded regions. By modelling a tape-spring analogously as

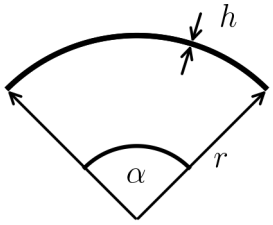

Figure 11: Tape-spring cross-section geometry.

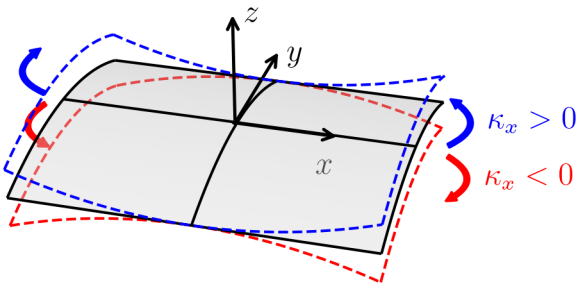

Figure 12: Deformation of an element of tape-spring under equal ($\kappa_x < 0$) and opposite ($\kappa_x > 0$) sense bending

a regularised Ericksen bar (derived from Guinot et al.[13] and Picault et al.[14]), they were able to confirm earlier results in [7] such as the propagating fold moment, and also obtain good estimates of the length of the ploy regions between the fold and unfolded regions of tape-spring, and whether one, or two or more folds would form.

It should be noted that for equal sense bending, torsional buckling occurs prior to phase separation, before the peak analytical moment is reached, thus allowing the tape-spring to bypass the energy barrier and separate into the two phases at a lower moment. The interaction of the torsional instability and phase separation is not covered here, but is worthy of further study.

Instead, we shall focus on showing that various analytical predictions of the fold radius are in fact approximations to the Maxwell Equal-Areas Construction; furthermore, by then solving the construction directly, an improved prediction is obtained. Fig. 12 illustrates the utilised sign convention. Curvature is defined according to $\kappa_x = d^2z/dx^2$, $\kappa_y = d^2z/dy^2$ where z are displacements of the deformed surface, with negative κ_x (resulting in a "mudguard" shape) corresponding to equal-sense bending, and positive κ_x, opposite-sense. The section bending moment, as illustrated by the blue arrows, is defined positive in opposite sense bending. Figure 13 illustrates the appearance of folds, typically forming in the middle of the tape-spring if one applies equal and opposite moments to either end.

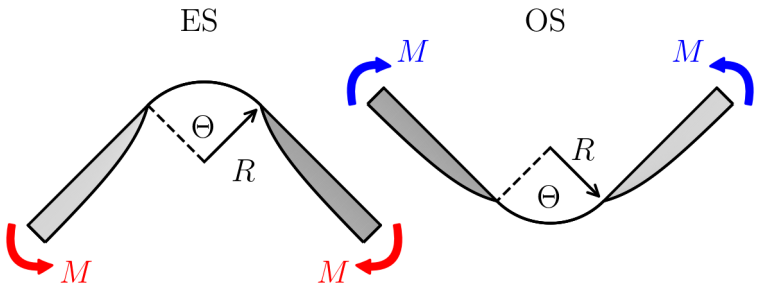

Figure 13: Tape-spring fold geometry in equal and opposite sense bending, with fold radius $R = 1/\kappa_x$, and flattened cross-section within the fold: M is the applied bending moment, which is also the fold-moment.

3.1 Rimrott analysis

Under Rimrott's assumption of a flat cross-section within the fold, Gaussian curvature of the surface is preserved and thus there is zero "stretching" strain energy due to mid-surface, in-plane strains. The bending strain energy per unit length is:

$$u = \frac{1}{2} Db \left[\kappa_x^2 \pm \frac{2\nu\kappa_x}{r} + \frac{1}{r^2} \right] \tag{19}$$

with $\pm$ for opposite and equal-sense bending respectively. It is assumed that the strain energy associated with the unfolded regions is negligible, and the strain energy in the ploy transition regions is constant and can be neglected: thus, assuming some fold angle Θ as illustrated in Fig. 13, the total strain energy is obtained by multiplying Eqn 19 by the requisite fold length $L = \Theta R = \Theta/\kappa_x$:

$$U = \frac{1}{2} \frac{\Theta Db}{\kappa_x} \left[\kappa_x^2 \pm \frac{2\nu\kappa_x}{r} + \frac{1}{r^2} \right] = \frac{1}{2} \Theta Db \left[\kappa_x \pm \frac{2\nu}{r} + \frac{1}{\kappa_x r^2} \right] \tag{20}$$

Minimising Eqn 20 with respect to κ_x leads straightforwardly to $\kappa_x = \pm 1/r$.

3.1.1 Effective Rimrott moment

The exact analytical solution for the strain energy per unit length in tape-spring bending (in the absence of torsional buckling), as given by Wuest [15] and Mansfield [16], is

$$u = \frac{Eh^3 b}{24} \left[\kappa_x^2 + \frac{(\nu\kappa_x + \kappa_{y0})^2 \left[1 - P_1(\lambda) \right]}{(1 - \nu^2)} \right] \tag{21}$$

with the bending moment given by

$$M = \frac{Db}{r} \left[(r\kappa_x + \nu) - \nu \left(1 + \nu r \kappa_x \right) P_1(\lambda) + \frac{\left(1 + \nu r \kappa_x \right)^2}{r\kappa_x} P_2(\lambda) \right] \tag{22}$$

where

$$\lambda = \sqrt[4]{3(1 - \nu^2)} \sqrt{\frac{b^2 \kappa_x}{h}}$$

and

$$P_1(\lambda) = \frac{2(\cosh(\lambda) - \cos(\lambda))}{\lambda(\sinh(\lambda) + \sin(\lambda))}, \quad P_2(\lambda) = -\frac{\sinh(\lambda)\sin(\lambda)}{(\sinh(\lambda) + \sin(\lambda))^2} + \frac{\cosh(\lambda) - \cos(\lambda)}{2\lambda(\sinh(\lambda) + \sin(\lambda))} \tag{23}$$

An important dimensionless parameter is $\beta = rh/b^2$, which can be thought of as the product of the "flatness", $r/b = 1/\alpha$, and the relative thickness, h/b: as β increases, the tape-spring becomes flatter and thicker, more resembling a plate; as β decreases the tape-spring becomes more characteristically "shell-like". Small β tape-springs have a significant peak and subsequent softening in the opposite-sense bending moment; when β increases, this peak decreases, and the bending response closer resembles that of a flat plate. Noting that λ can be written as

$$\lambda = \sqrt[4]{3(1 - \nu^2)} \sqrt{\frac{\kappa_x r}{\beta}}$$

the dimensionless bending moment Mr/Db is therefore a function of the dimensionless curvature $\kappa_x r$, ν, and β.

Rimrott's analysis can now be shown equivalent to an application of the Maxwell Equal-Areas Construction. Consider the behaviour of Eqn 22 as $\beta \to 0$, for opposite sense bending, see Fig. 14. As β decreases, the peak non-dimensional moment increases, tending towards infinity, whilst the rest of the solution converges to the moment of a completely flattened tape-spring, equal to

$$\frac{Mr}{Db} = \kappa_x r + \nu \tag{24}$$

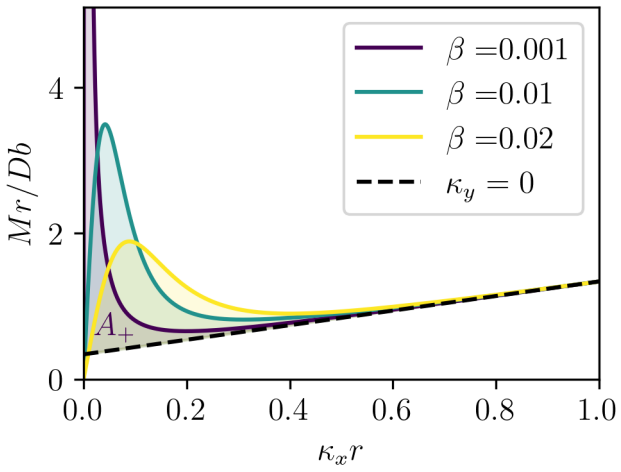

Figure 14: Analytical solution for decreasing β. The dashed line indicates the moment for a completely flattened tape-spring.

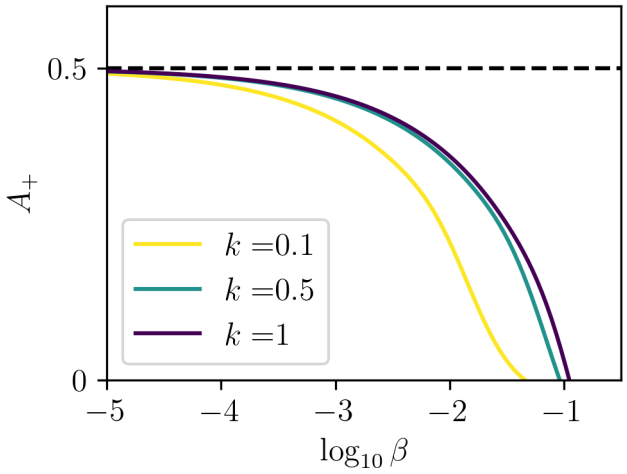

Figure 15: Evaluation of A_+ for decreasing β and different upper limits k.

It is worth investigating what happens to the shaded area in Fig. 14 between the full analytical solution and the flattened moment solution, given by

$$A_+ = \int_0^{\kappa_x r = k} \frac{Mr}{Db} - (\kappa_x r + \nu)\, \mathrm{d}\kappa_x r \tag{25}$$

where k is an upper limit to be confirmed shortly as any value. In dimensionless form, the strain energy per unit length, Eqn 21, can be written as

$$\frac{ur^2}{Db} = \frac{1}{2}(1-\nu^2)(\kappa_x r)^2 + \frac{1}{2}(\nu\kappa_x r + 1)^2\,[1 - P_1(\lambda)] \tag{26}$$

$A_+(k)$ is therefore given by

$$\begin{aligned} A_+(k) =& \frac{1}{2}(1-\nu^2)k^2 + \frac{1}{2}(\nu k + 1)^2\,[1 - P_1(\lambda)] - \left(\nu k + \frac{1}{2}k^2\right) \\ =& \frac{1}{2} - \frac{1}{2}(\nu^2 k^2 + 2\nu k + 1)P_1(\lambda) \end{aligned} \tag{27}$$

As $\beta \to 0$, then $\lambda \to \infty$ and $P_1(\lambda) \to 0$, thus A_+ tends to a value of 0.5 for any value of k.

Fig. 15 plots the value of this area evaluated for a range of β and k, clearly showing that the limiting value of A_+, as β tends to zero, is 0.5. One can also deduce the value of A_+ from Rimrott's expression for the strain energy per unit length of tape-spring fold, Eqn 19, which in non-dimensional form is

$$\frac{ur^2}{Db} = \frac{1}{2}(\kappa_x r)^2 + \nu\kappa_x r + 0.5 \tag{28}$$

We can now describe an "effective Rimrott moment", whose integral is Rimrott's approximate strain energy, by use of a Dirac delta function:

$$\frac{Mr}{Db} = \kappa_x r + \nu + 0.5\delta(0) \tag{29}$$

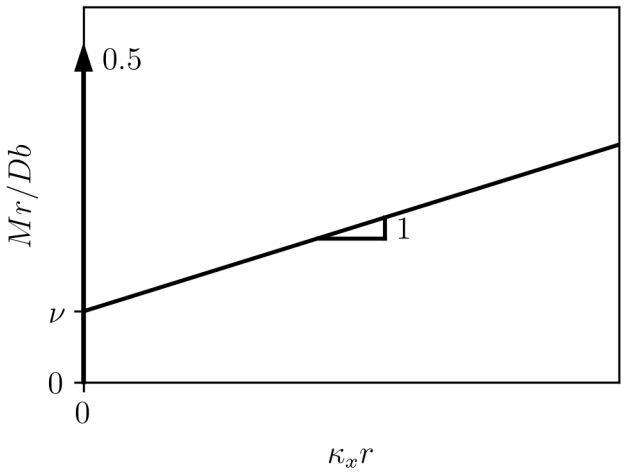

Figure 16: "Effective Rimrott moment"

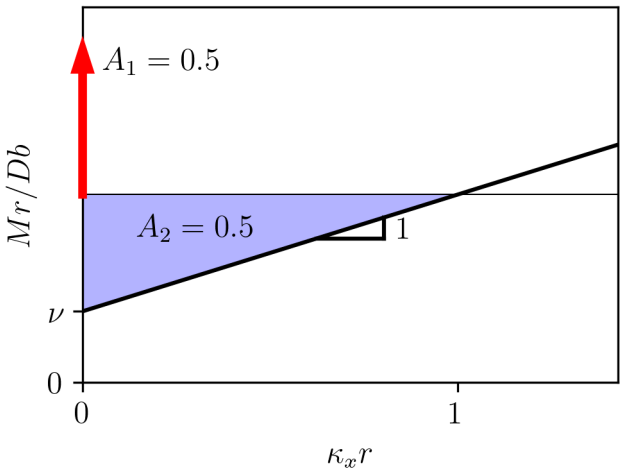

Figure 17: Maxwell Equal-Areas Construction applied to the effective Rimrott moment

The Maxwell Equal-Areas Construction may be directly applied to the effective Rimrott moment to obtain the fold curvature, as illustrated in Fig. 17. Given the Dirac delta function has infinite height, the area contained beneath it lies, in effect, far above any equal area line, thus whatever the position of said line, $A_1 = 0.5$. Therefore we simply need to find $A_2 = 0.5$, which, given the moment gradient of 1, occurs when the equal area line intercepts at $\kappa_x r = 1$. Equivalently, the formulation of the Maxwell Equal-Areas Construction given in Eqn 14 leads to the same conclusion in a slightly more rigorous manner.

3.2 Calladine & Seffen analysis

Seffen [17] observed from finite element analysis and physical experiments that the Rimrott prediction of fold curvature was an overestimate, particularly in opposite-sense bending, where the error was up to 15% for some tape-springs. The reason for this, expounded in an improved analysis, is offered by Calladine & Seffen [6], who noted that the fold strain energy in the Rimrott analysis, which assumes a completely flat cross-section, is overestimated because the cross-section is "relieved" of an edge moment: there is a small boundary region along each edge where non-zero curvature is required to satisfy the zero edge moment boundary condition. They introduce

a "reduced" strain energy function, taking account of the boundary region, written as in present notation:

$$U_R = \frac{Db\Theta}{2r}\left[\kappa_x r + \frac{1}{\kappa_x r} \pm 2\nu - A\left((\kappa_x r)^{-3/2} + \nu^2(\kappa_x r)^{1/2} \pm 2\nu(\kappa_x r)^{-1/2}\right)\right] \tag{30}$$

Minimising with respect to κ_x, the fold curvature is thence predicted to be $\kappa_x = \pm\kappa_{y0}/\xi$, where ξ is given by the solution of a characteristic equation:

$$1 - \frac{1}{\xi^2} - \frac{A}{2}\left[3\xi^{1/2} - \frac{\nu^2}{\xi^{3/2}} \pm \frac{2\nu}{\xi^{1/2}}\right] = 0 \tag{31}$$

where $\pm$ corresponds to opposite and equal-sense bending, respectively, and A is a constant given by

$$A = \frac{2}{[3(1-\nu^2)]^{1/4}}\frac{1}{T} \tag{32}$$

and T is a non-dimensional parameter similar to β:

$$T = \sqrt{\frac{b^2}{rh}} = \frac{1}{\sqrt{\beta}} \tag{33}$$

It can be seen that in the small β/large T limit, $A \to 0$ and Rimrott's solution $\xi = 1$ is recovered, as expected from the effective Rimrott moment analysis. In this limit the size of the edge boundary layer diminishes to zero and Rimrott's strain energy expression matches the exact solution.

3.2.1 Link with Common Tangent Construction

Rimrott's anlaysis takes a simplified expression for the strain energy per unit length u, multiplies it by the fold length, and minimises with respect to the fold curvature. Disregarding various constants, it is essentially a minimisation of $uR = u/\kappa_x$ where the expression for u is approximate. Calladine & Seffen improve the analysis by determining a more accurate expression for the strain energy u. It is worth noting this analysis can be done numerically, using Wuest's exact analytical expression for u. Differentiating u/κ_x with respect to κ_x gives

$$\frac{\mathrm{d}}{\mathrm{d}\kappa_x}\left(\frac{u}{\kappa_x}\right) = \frac{\kappa_x \cdot \mathrm{d}u/\mathrm{d}\kappa_x - u}{\kappa_x^2} \tag{34}$$

Setting this equal to zero leads to the condition

$$\frac{\mathrm{d}u}{\mathrm{d}\kappa_x} = \frac{u}{\kappa_x} \tag{35}$$

which is, in fact, equivalent to the Common Tangent Construction if $(\kappa_{xA}, u_A) = (0, 0)$, which is approximately the case for most tape-springs with small β. Thus, Calladine & Seffen's analysis is an approximation to the Maxwell Equal-Areas Construction, accurate for small β but increasingly less so as β increases.

3.2.2 Improved analysis

It is possible to improve upon Calladine & Seffen's analysis by directly solving the Common Tangent Construction, thus taking account of the unfolded regions of tape-spring. By dividing the reduced strain energy U_R by the fold length Θ/κ_x, we obtain the strain energy per unit length in the fold, which is analogous to u_B in the Common Tangent Construction:

$$u_B = \frac{Db}{2r^2}\left[\kappa_{xB}^2 r^2 + 1 \pm 2\nu\kappa_{xB} r - A\left((\kappa_{xB} r)^{-1/2} + \nu^2(\kappa_{xB} r)^{3/2} \pm 2\nu(\kappa_{xB} r)^{1/2}\right)\right] \tag{36}$$

The fold moment can be derived from u_B:

$$M = \frac{\mathrm{d}u_B}{\mathrm{d}\kappa_{xB}} = \frac{Db}{r}\left[\kappa_{xB} r \pm \nu - A\left(-\frac{1}{4}(\kappa_{xB} r)^{-3/2} + \frac{3}{4}\nu^2(\kappa_{xB} r)^{1/2} \pm \frac{\nu}{2}(\kappa_{xB} r)^{-1/2}\right)\right] \tag{37}$$

The first part inside the bracket is recognisable as the Rimrott fold moment, $M = Db[\kappa_{xB} \pm \nu/r]$, with the terms proportional to A deriving from the Calladine & Seffen correction.

We now require expressions for for the curvature κ_{xA} and strain energy u_A in the unfolded regions. As with the previous analyses, solution of the Common Tangent Construction neglects the ploy region and assumes an instantaneous transition from folded to unfolded regions. In these regions, the cross-section is relatively undeformed, thus can be treated as an Euler-Bernoulli beam with bending moment

$$M = EI\kappa_{xA} \tag{38}$$

and strain energy

$$u_A = \frac{1}{2}EI\kappa_{xA}^2 \tag{39}$$

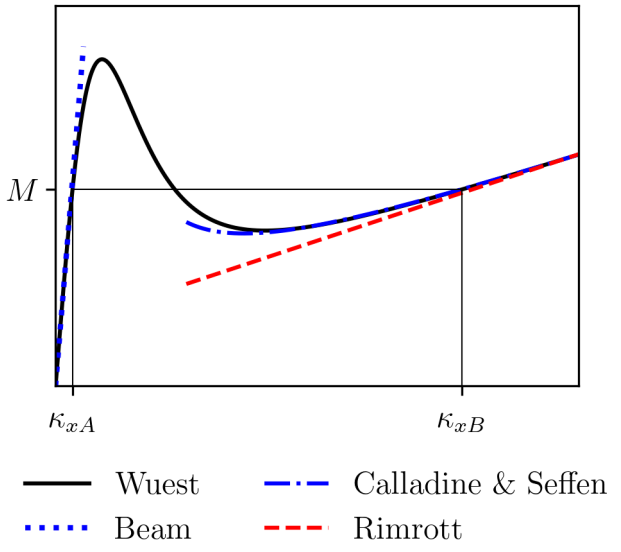

Figure 18: Moment approximations

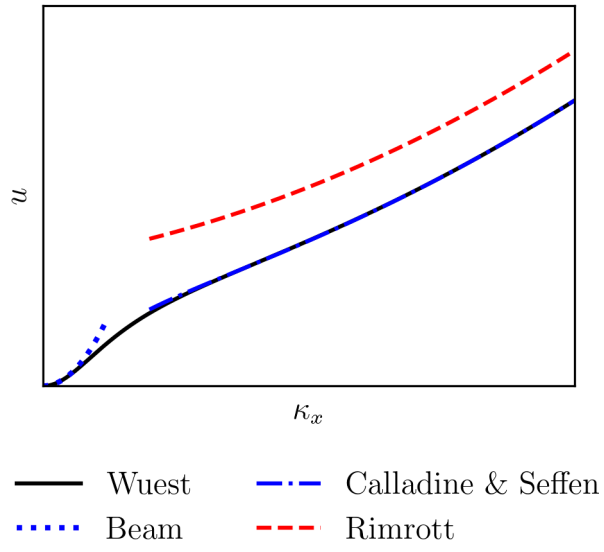

Figure 19: Strain energy approximations

By equating the moments in the folded and unfolded regions, it will be possible to obtain κ_{xA} as a function of κ_{xB}. Figure 18 plots the full analytical moment solution (Wuest), the Rimrott and

Calladine & Seffen fold moment approximations, and the beam approximation for the unfolded regions, whilst Fig. 19 plots the corresponding strain energies.

The beam solution is a good approximation to the full solution for small curvatures. It can also be seen that whilst the Calladine & Seffen solution provides a far more accurate strain energy than Rimrott, the difference in bending moment is minimal. Therefore, it makes sense to use the (much simpler) Rimrott fold moment to obtain an expression for κ_{xA}:

$$\kappa_{xA} = \frac{Db}{EIr}[\kappa_{xB} r \pm \nu] \tag{40}$$

Substitution into u_A gives

$$u_A = \frac{D^2 b^2}{2EIr^2}[\kappa_{xB} r \pm \nu]^2 \tag{41}$$

Substitution of κ_{xA}, κ_{xB}, u_A, u_B, and $du_B/d\kappa_{xB}$ into the Common Tangent Construction yields

$$\frac{bD}{2r^2}\left[\kappa_{xB}^2 r^2 + 1 \pm 2\nu\kappa_{xB} r - A\left((\kappa_{xB} r)^{-1/2} + \nu^2(\kappa_{xB} r)^{3/2} \pm 2\nu(\kappa_{xB} r)^{1/2}\right)\right] - \frac{D^2 b^2}{2EIr^2}[\kappa_{xB} r \pm \nu]^2$$
$$-\frac{bD}{r}\left[\kappa_{xB} r \pm \nu - A\left(-\frac{1}{4}(\kappa_{xB} r)^{-3/2} + \frac{3}{4}\nu^2(\kappa_{xB} r)^{1/2} \pm \frac{\nu}{2}(\kappa_{xB} r)^{-1/2}\right)\right]\left[\kappa_{xB} - \frac{Db}{EIr}[\kappa_{xB} r \pm \nu]\right] = 0 \tag{42}$$

The second moment of area of a tape-spring is

$$I = \frac{r^3 h}{2\alpha}\left[\alpha^2 - 4(1 - \cos\alpha) + \alpha\sin\alpha\right] \tag{43}$$

however this can be simplified for shallow cross-sections to

$$I = \frac{b^5 h}{720 r^2} \tag{44}$$

To simplify the expressions, introduce a new constant B such that

$$B = \frac{Db}{EI} = \frac{60}{(1-\nu^2)}\frac{1}{T^4} \tag{45}$$

and finally, after some manipulation, formulating in terms of $\xi = 1/\kappa_{xB} r$, yields the following equation for ξ:

$$1 - \frac{1}{\xi^2} - \frac{A}{2}\left[3\xi^{1/2} - \frac{\nu^2}{\xi^{3/2}} \pm \frac{2\nu}{\xi^{1/2}}\right] + \underbrace{B\left[\frac{1}{\xi} \pm \nu\right]\left[\frac{1}{\xi} \pm \nu - \frac{A}{2}\left(\frac{3\nu^2}{\xi^{1/2}} - \xi^{3/2} \pm 2\nu\xi^{1/2}\right)\right]}_{\text{Correction}} = 0 \tag{46}$$

This of course must be solved numerically as per Eqn 31. The first half of the equation is identical to Calladine & Seffen's, with the second half, proportional to B, providing a correction accounting for the unfolded regions. As $A \propto 1/T$, and $B \propto 1/T^4$, it follows that: for very large T, both A and B can be neglected, and the equation reduces to the Rimrott solution ($\xi = 1$); for intermediate T, only B can be neglected and the Calladine & Seffen solution is adequate; for small T, the full solution is required. It is worth briefly noting that the characteristic length of the ploy region, L_p [19], is

$$\frac{L_p}{b} = \frac{2}{\pi}\left[3(1-\nu^2)\right]^{1/4} T \tag{47}$$

Thus, as T decreases, the length of the ploy region decreases, and the boundary becomes sharper, approaching the idealised Maxwell construction analysis.

3.3 Comparison of all solutions

Figure 20(a) compares the solutions which minimise u/κ_x, both a numerical implementation of Eqn 35 ($\times$) and Calladine & Seffen's analytical solution ($-$), to solutions which solve the Maxwell Equal-Areas Construction, both a numerical implementation ($-\cdot$) and the improved analytical solution ($\cdot\cdot$), and to Calladine & Seffen's finite element results ($\bullet$), over the range of T considered in Calladine & Seffen's paper.

There is good agreement between all solutions, with the finite element results agreeing perfectly with the Equal-Areas solutions, and the u/κ_x minimisation solutions lying ever so slightly above, most notably for $T = 10.5$; this suggests the Equal-Areas solutions are more accurate, as one would expect.

To check this, Fig. 20(b) extends the plot to smaller values of T, i.e. relatively flatter and thicker tape-springs. The commercial finite element software package, Abaqus FEA [18], is used to obtain FE results, where tape-springs are modelled with S4R5 reduced integration shell elements, and a stabilised static general step used during a non-linear analysis. Here, the differences between the solutions become apparent. The Equal-Areas solutions continue to agree nearly perfectly with the FE results, with only minor difference observed in the $T = 6$ analytical solution. Meanwhile the divergence of the u/κ_x minimisation solutions is evident, most notably for $T = 6$ where there is a near 10% difference in ξ for opposite sense bending (highlighted by the arrow), though in equal sense bending the differences are less pronounced.

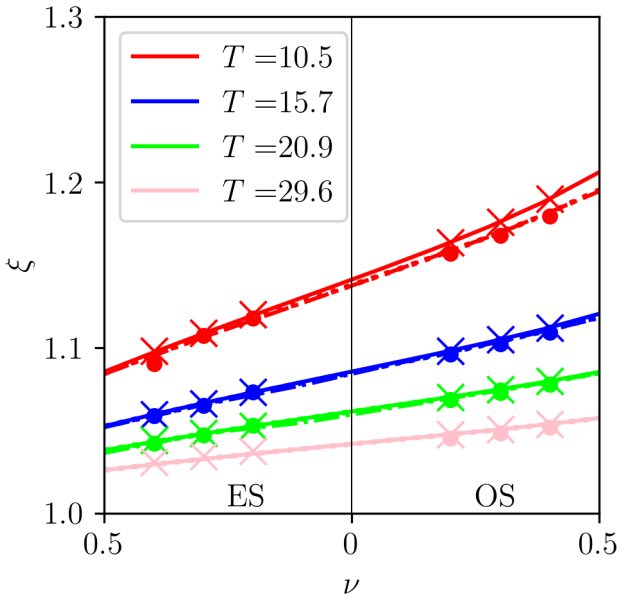

(a) Values of T discussed in [6]. Note that numerical evaluation of the Maxwell Equal-Areas Construction becomes difficult for large T, and thus was not possible for $T = 29.6$.

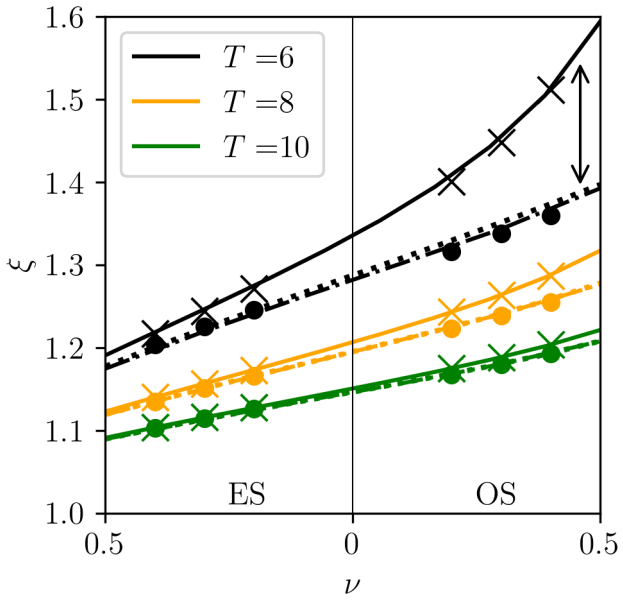

(b) Smaller T/larger β (i.e. thicker and flatter tape-springs) than discussed in [6]. Discrepancy between the minimisation and Equal-Areas solutions for $T = 6$ is highlighted by the arrow.

Figure 20: ξ obtained via different methods. Solid curves plot Calladine & Seffen's analytical minimisation; crosses, numerical minimisation; dotted curves, analytical Maxwell Equal-Areas Construction; dash-dotted curves, numerical Maxwell Equal-Areas Construction; circles, finite element results.

Solution which minimise u/κ_x lose validity for tape-springs with smaller T as they fail to consider the contribution to strain energy and total angle subtended from the unfolded regions of the tape-spring. As can be see in in Fig. 21, for tape-springs with large T the curvature in the regions outside the fold, and thus strain energy in those regions, is negligible in comparison to the fold curvature. For these tape-springs, minimising the total strain energy is nearly equivalent to minimising the strain energy in the folded region. By contrast, for tape-springs with smaller T, as exemplified in Fig. 22, the curvature in the regions outside the fold is non-negligible in comparison to the fold curvature, thus to accurately determine the fold curvature it is essential to minimise the strain energy in the whole tape-spring.

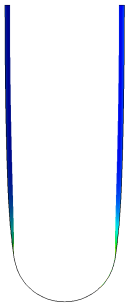

Figure 21: Tape-spring with $T = 10$, $\nu = 0.2$. in opposite sense bending.

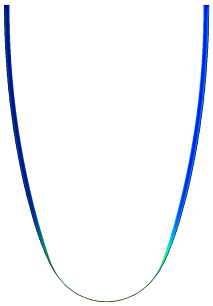

Figure 22: Tape-spring with $T = 6$, $\nu = 0.2$. in opposite sense bending.

4 Conclusions

Elastic localisation has been explained with reference to thermodynamic phase transitions and propagating instabilities. These offer two different ways of considering the problem: as one of energy minimisation or of internal and external work balance, which are in fact equivalent. Both analyses show that the Maxwell Equal-Areas Construction determines the strain in each phase. A new proof for the Maxwell Equal-Areas Construction is shown.

Tape-spring folds have been investigated as an example of elastic localisation. The Rimrott prediction that the fold radius is equal to the initial transverse radius is shown to be equivalent to an application of the Maxwell Equal-Areas Construction in the limit of zero thickness. The Calladine & Seffen fold radius prediction is shown to be an approximation of the Common Tangent Construction, and an improvement is made by consideration of the unfolded regions, resulting in excellent agreement with finite element results.

The torsional buckling associated with the equal sense bending of tape-springs has not been covered in this study. The interaction between the torsional instability and fold formation is of considerable interest, as the torsional mode enables the tape-spring to achieve phase separation while bypassing the peak moment observed in opposite sense bending; there is no meta-stable state observed. The manner in which this occurs is worthy of future investigation.

The authors would like to thank the EPSRC and StructureMode for funding this research through the EPSRC Centre for Doctoral Training in Future Infrastructure and Built Environment: Resilience in a Changing World (EPSRC grant reference number EP/S02302X/1).

References

[1] J Clerk-Maxwell, On the Dynamical Evidence of the Molecular Constitution of Bodies, (1875) *Journal of the Chemical Society*, 28(0), pp. 493–508

[2] J D Van der Waals, Over de Continuiteit van den Gas-en Vloeistoftoestand, (1873) *Ph.D. Thesis, University of Leiden, Leiden.*

[3] J L Ericksen, Equilibrium of bars, (1975) *Journal of Elasticity*, 5(3-4), pp. 191–201

[4] L Truskinovsky and G Zanzotto, Ericksen's bar revisited : Energy wiggles, (1996) *Journal of the Mechanics and Physics of Solids*, 44(8), pp. 1371-1408

[5] F P J Rimrott, Querschnittsverformung bei Torsion Offener Profile, (1970) *ZAMM-Journal of Applied Mathematics and Mechanics/Zeitschrift für Angewandte Mathematik und Mechanik*, 50(12), pp. 775-778

[6] C R Calladine and K A Seffen, Folding the Carpenter's Tape: Boundary Layer Effects, (2020) *Journal of Applied Mechanics*, 87(1), pp. 011009-1-5

[7] K A Seffen and S Pellegrino, Deployment dynamics of tape-springs, (1999) *Proceedings of the Royal Society of London. Series A: Mathematical, Physical and Engineering Sciences*, 455(1983), pp. 1003-1048

[8] E Chater and J W Hutchinson, On the Propagation of Bulges and Buckles, (1984) *Journal of Applied Mechanics*, 51(2), pp. 269–277

[9] C Lestringant and B Audoly, A Diffuse Interface Model for the Analysis of Propagating Bulges in Cylindrical Balloons, (2018) *Proceedings of the Royal Society of London. Series A: Mathematical, Physical and Engineering Sciences*, 474(2218), pp. 20180333

[10] M E Gurtin, Two-phase deformations of elastic solids, (1983) *Archive for Rational Mechanics and Analysis*, 84(1), pp. 1-29

[11] C R Calladine, The Theory of Thin Shell Structures 1888–1988, (1988) *Proceedings of the Institution of Mechanical Engineers, Part A: Power and Process Engineering*, 202(3), pp. 141-149

[12] M Martin and S Bourgeois and B Cochelin and F Guinot, Planar folding of shallow tape-springs: The rod model with flexible cross-section revisited as a regularized Ericksen bar model, (2020) *International Journal of Solids and Structures*, 188-189, pp. 189-209

[13] F Guinot and S Bourgeois and B Cochelin and L Blanchard, A planar rod model with flexible thin-walled cross-sections. Application to the folding of tape-springs, (2012) *International Journal of Solids and Structures*, 49(1), pp. 73-86

[14] E Picault and P Marone-Hitz and S Bourgeois and B Cochelin and F Guinot, A planar rod model with flexible cross-section for the folding and the dynamic deployment of tape-springs: Improvements and comparisons with experiments, (2014) *International Journal of Solids and Structures*, 51(18), pp. 3226-3238

[15] W Wuest, Einige Anwendungen der Theorie der Zylinderschale, (1954) *ZAMM-Journal of Applied Mathematics and Mechanics/Zeitschrift für Angewandte Mathematik und Mechanik*, 34(12), pp. 444-454

[16] E H Mansfield, Large-Deflexion Torsion and Flexure of Initially Curved Strips, (1973) *Proceedings of the Royal Society of London. Series A*, 334(1598), pp. 279-298

[17] K A Seffen, On the Behaviour of Folded Tape-Springs, (2000) *Journal of Applied Mechanics*, 68(3), pp. 369–375

[18] M Smith, ABAQUS/Standard User's Manual, Version 6.9., (2009) *Dassault Systèmes Simulia Corp*

[19] B Wang and K A Seffen and S D Guest, Folding of Bistable Composite Tape-Springs, (2019) CUED/D-STRUCT/TR.252

[20] K Miura and S Pellegrino, *Forms and Concepts for Lightweight Structures*, (2020) Cambridge University Press

[21] J M Fernandez and M Schenk and G Prassinos and V J Lappas and S O Erb, Deployment Mechanisms of a Gossamer Satellite Deorbiter, (2013) *Paper presented at 15th European Space Mechanisms and Tribology Symposium*

[22] J M Fernandez and A Viquerat and V J Lappas and A J Daton-Lovett, Bistable Over the Whole Length (BOWL) CFRP Booms for Solar Sails, (2014) *Advances in Solar Sailing*, pp. 609-628

List of Figures